Continuum-micromechanics approach for determination of autogenous shrinkage of cement-based materials

Ch. Pichler, R. Lackner, & H.A. Mang
Institute for Strength of Materials, Vienna University of Technology, Austria

ABSTRACT: Autogenous shrinkage is the term for the bulk deformation of a closed, isothermal, cement-based material system not subjected to external forces (Jensen and Freiesleben Hansen 2001). It is associated with the internal volume reduction of the cement/water mixture in the course of the hydration process. The question arising from engineering practice is the magnitude of the autogenous deformation of different cement-based materials, such as shotcrete employed in tunneling or high-performance concrete. Whereas autogenous shrinkage in shotcrete linings results in a significant reduction of compressive loading, restrained autogenous deformation in high-performance concrete may lead to cracking. In this paper, a multi-scale approach, allowing to consider induced strains at lower scales of observation, is presented. In addition to the theoretical work on multi-scale modeling, macroscopic shrinkage experiments on cement pastes were conducted at the Vienna University of Technology.

Keywords: early-age concrete, multi scale, homogenization, eigenstrain, capillary depression, pore structure

1 PHYSICAL ORIGIN OF AUTOGENOUS SHRINKAGE

Autogenous shrinkage is associated with the internal volume reduction of the cement/water mixture caused by the hydration process. The volumetric imbalance is depicted in Figure 1 [adapted from (Acker 2001)]: the specific volume of the reaction products [calcium-silicate-hydrates (CSH) and portlandite (CH)] is about 8% lower than the sum of the volumes of the reactants (water, cement, and additiva), a behavior also referred to as *Le Chatelier* contraction. In Figure 1, ξ denotes the degree of hydration, with $\xi = f_h/f_{h,\infty}$, where f_h is the volume fraction of hydration products and $f_{h,\infty}$ is the respective quantity in case the entire amount of cement has been consumed by the hydration process. The volumetric imbalance of 8% results in a progressive increase of the pore volume filled with gaseous phase (see Figure 1). On the other hand, the relative pore volume occupied by the liquid phase, i.e., the liquid saturation, decreases in the course of the hydration process (see Figure 1). The stress state in the liquid phase follows the law of surface tension: the smaller the pore size, the larger the tension at the interface between liquid and gaseous phase. As the degree of liquid saturation (relative pore volume occupied by the liquid phase) decreases, the location of this interface moves into smaller pores, resulting in an increase of surface (capillary) tension in the liquid phase. This tension in the liquid phase causes a contraction of the solid phase (unhydrated cement and reaction products), which is macroscopically observable as autogenous-shrinkage strain (Acker and Ulm 2001). Experimental observations suggest that the magnitude of the capillary tension is mainly influenced by the water/cement-ratio, defining the pore structure of the cement paste (Acker 2001).

2 EXPERIMENTAL BASIS

2.1 *Hydration kinetics*

As mentioned in the previous section, the extent of the hydration process, i.e., of the chemical reaction between cement and water, is described by the degree of hydration ξ, with $0 \le \xi \le 1$. A suitable evolution law for the hydration kinetics may be written in the form (Ulm and Coussy 1995):

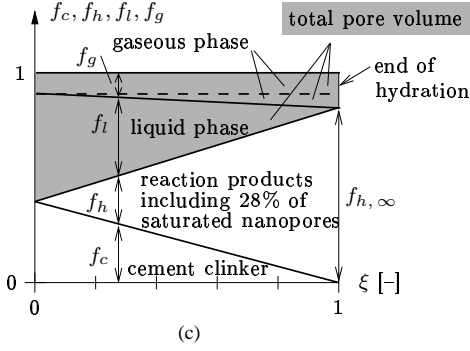$$\dot{\xi} = \tilde{A}(\xi)\exp\left(-\frac{E_a}{RT}\right) , \qquad (1)$$

Figure 1: Variation of volume fractions for cement pastes with $w/c = \overline{w/c} = 0.425$ [adapted from (Acker 2001)]

where E_a, R, and T denote the activation energy of the employed cement, the universal gas constant, and the absolute temperature, respectively. The Arrhenius factor $\exp[-E_a/(RT)]$ accounts for the thermal activation of the hydration reaction. The normalized chemical affinity $\tilde{A}(\xi)$ represents the driving force of the hydration process, depending only on the hydration extent (Ulm and Coussy 1995). For the types of ordinary Portland cements (OPC) considered in the experimental program, the chemical affinity was computed from experimental results obtained from differential calorimetry (Toni-CAL I, Toni Technik, Berlin, Germany). Hereby, the heat flux out of the sample, $\dot{Q}(t)$ [J/s], is recorded, whereas the temperature in the calorimeter is kept constant (isothermal conditions).

Integrating the field equation for the thermochemical problem (Ulm and Coussy 1995) over the volume of the test sample, specialized for isothermal conditions, one gets

$$-L_\xi \dot{\xi}(t) = -\dot{Q}(t) \ \Rightarrow \ \xi(t) = \frac{Q(t)}{L_\xi}, \quad (2)$$

where L_ξ [J] denotes the heat of hydration of the cement considered in the test sample. Inserting $\dot{\xi} = \dot{Q}/L_\xi$ (Equation (2)) into Equation (1) yields the evolution of the the chemical affinity as

$$\tilde{A}(t) = \frac{\dot{Q}(t)}{L_\xi \exp[-E_a/(RT)]} \ \ [1/s]. \quad (3)$$

Combination of $\xi(t)$ and $\tilde{A}(t)$ as computed from Equations (2) and (3) gives access to the chemical-affinity function $\tilde{A}(\xi)$. Figure 2 depicts $\tilde{A}(\xi)$ obtained for ordinary Portland cement (OPC) characterized by a w/c-ratio of 0.42 and various *Blaine* (grinding) fineness. In Equation (3), L_ξ was computed from the amount of cement (in [g]) multiplied

by 400 J/g [see, e.g., (Ballim and Graham 2003)], E_a/R was set equal to 4000 K (Freiesleben Hansen and Pedersen 1977), and T is set equal to the constant temperature of 303 K throughout the experiment.
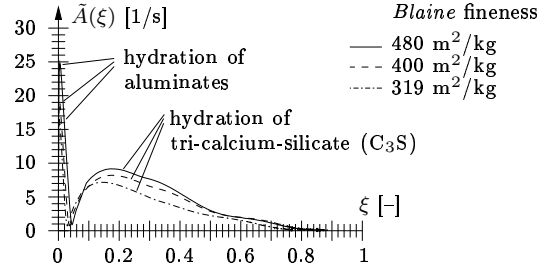

Figure 2: Normalized chemical affinity $\tilde{A}(\xi)$ of OPC obtained from differential calorimetry

2.2 *Autogenous-shrinkage measurements*

Figure 3 depicts test results for the autogenous shrinkage strain ε^s obtained from a uniaxial test setup proposed by (Jensen and Freiesleben Hansen 1995). For all shrinkage experiments, the temperature in the specimen was kept constant at 19°C. The circle in Figure 3 marks the time instant of the percolation threshold, t_0, also referred to as setting time, i.e., the time instant when the solid phases in the material become interconnected. For $t < t_0$, the cement paste can shrink freely and, hence, the *Le Chatelier* contraction is converted directly into a macroscopically observable shrinkage strain. In Figure 3, $t = 0$ refers to the time instant of water addition, whereas ε^s is set equal to zero at $t = t_0$. All specimens show a small expansion period right after setting which is explained by suction of bleed water back into the specimen. Figure 4 shows ε^s as a function of the degree of hydration ξ. Hereby, the history of ξ was obtained from numerical integration of Equation (1), using $\tilde{A}(\xi)$ depicted in Figure 2 and $T = 292$ K.
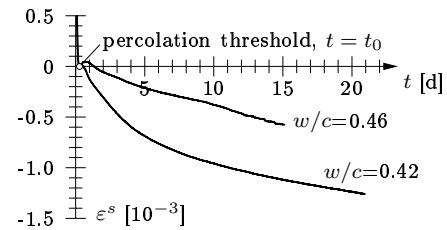

Figure 3: History of autogenous-shrinkage strain of OPC with a *Blaine* fineness of 480 m²/kg obtained from uniaxial experiments
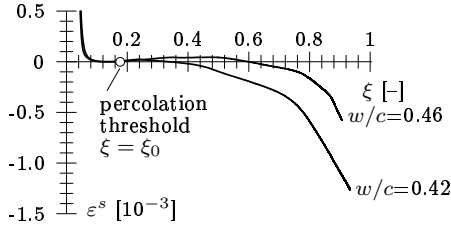
Figure 4: Autogenous-shrinkage strain as a function of ξ for OPC with a *Blaine* fineness of 480 m^2/kg

2.3 *Pore structure and capillary depression*

In this subsection, a model for the prediction of the pore size distribution of hardening cement paste is developed, giving access to the capillary depression in the pore liquid. In the context of multiscale modeling, the so-obtained capillary depression will be considered as loading in the liquid phase (see Subsection 3.3).

In partially-saturated cement pastes, the pressure difference along the liquid-gas interface, Δp [Pa], is given by the generalized *Young-Laplace equation* (Gaydos et al. 1996):

$$\Delta p = \gamma_{12} \left(\frac{1}{R_1} + \frac{1}{R_2} \right) + C_H \frac{1}{R_1 R_2} \, , \quad (4)$$

where R_1 [m] and R_2 [m] are the principal radii of curvature of the liquid-gas interface and γ_{12} [N/m] is the interfacial tension between two non-solid, immiscible substances. C_H [Nm/m] is the flexural stiffness. Since the radii R_1 and R_2 depend on the pore size, experimental techniques are required for determination of the pore-size distribution of hydrating cement. In the past, three different experimental techniques were developed:

- Mercury intrusion porosimetry (MIP) is characterized by the quasi-static injection of a pressurized, nonwetting fluid (mercury) into the cement paste. All evaporable pore water is removed from the pores prior to the test. MIP provides the intruded volume as a function of the applied mercury pressure. Based on the assumptions of (a) a cylindrical shape of the intruded pores and (b) a decreasing pore size with increasing distance from the outer surface of the specimen (accessibility, see case (i) in Figure 5), the intruded pore diameter at a certain mercury pressure and, furthermore, the relative pore-size distribution can be computed from the intruded volume – mercury pressure relation. Unfortunately, assumption (b) cannot be confirmed by microscopic techniques (Diamond 2000). A great portion of larger capillary

pores is located inside the specimen and can only be reached by mercury through a chain of smaller pores of various size and shapes (see cases (ii) and (iii) in Figure 5). Accordingly,
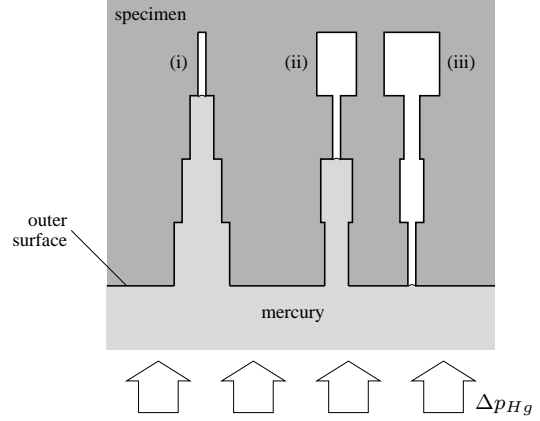

Figure 5: Accessibility of pores by MIP

these larger pores can only be intruded by mercury after applying a pressure which admits the intrusion of the smallest pore size encountered on that chain. The pore diameter corresponding to this pressure is referred to as "threshold" diameter. When passing the mercury pressure corresponding to the "threshold" diameter during MIP experiments, a steep increase of the intruded volume is observed. Despite the mentioned limitation of MIP, qualitative information can be extracted from experimental results, such as, e.g., the progressive refinement of the pore structure in the course of hydration (Diamond 2000). Moreover, once the pressure corresponding to the "threshold" diameter is exceeded, large capillary pores inside the specimen become filled and MIP gives the correct distribution for pore sizes smaller than the "threshold" diameter. In cement pastes characterized by low water content at an advanced state of the hydration process, the liquid-gas interface is located in this pore-size range.

Specialization of Equation (4) for a spherical-cap shaped meniscus, neglecting the flexural stiffness ($C_H = 0$), yields an expression for the principal radius of the mercury-gas interface:

$$R_{Hg} = \frac{2\gamma_{Hg,gas}}{\Delta p_{Hg}} \, , \quad (5)$$

with $\gamma_{Hg,gas} = 0.474$ N/m. Accounting for cylindrical pores and the different contact angles of mercury and water with cement, α_{Hg}

and α_w, respectively, the principal radius of the corresponding water-gas interface can be estimated as (see Figure 6)

$$R_w = R_{Hg}\frac{\cos\alpha_{Hg}}{\cos\alpha_w} = \frac{2\gamma_{Hg,gas}}{\Delta p_{Hg}}\frac{\cos\alpha_{Hg}}{\cos\alpha_w} \; . \tag{6}$$

Since α_w is negligibly small [$\alpha_w \approx 0°$, see, e.g., (Hua et al. 1995)], $2R_w$ can be set equal to the pore diameter at the location of the liquid-gas interface. Based on the given value of R_w
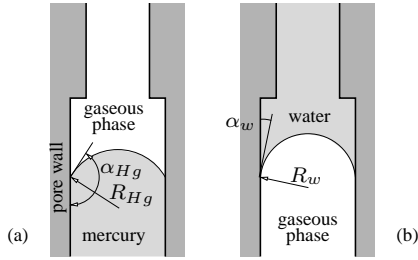

Figure 6: Principal radii and contact angles at (a) mercury-gas and (b) water-gas interfaces

[Equation (6)] for an intruded mercury volume equal to the gaseous volume of unprepared partially-saturated cement pastes, the capillary depression in these cement pastes can be computed from Equation (4) as

$$\Delta p_l = \frac{2\gamma_{w,gas}}{R_w} \; , \tag{7}$$

where $\gamma_{w,gas} = 0.073$ N/m.

- Nuclear magnetic resonance (NMR) [see (Hornak 2003) for a detailed description] is a phenomenon observed when the nuclei of certain atoms are immersed in a static magnetic field while exposing them to a second oscillating magnetic field. Under such magnetic-field conditions, some nuclei, including the protons of hydrogen in a water molecule, experience this phenomenon. One NMR measuring technique for the estimation of the pore size distribution exploits the decreasing freezing temperature of water embedded in capillary pores. Hereby, the temperature of the cement specimen is continuously reduced, while the NMR signal, which is associated with the liquid part of the water, is recorded. Finally, the known relationships between the freezing point depression and the pore size provide access to the pore-size distribution (Milia et al. 1998). Respective pore size distributions for a cement paste characterized by a w/c-ratio of 0.43 and a curing time of 122 d are reported in (Jehng et al. 1996).

- Image analysis of scanning-electron-microscopy (SEM) micrographs is characterized by embedding thin slices of cement paste in low viscosity epoxy resin, polishing the surface, and detecting the epoxy filled pores in the backscatter electron images (Diamond and Leeman 1995). Coverage of these pores is based on the different gray level of epoxy resin and the solid phase. The lower limit of detectable pores is bound to the SEM magnification and resolution of the micrographs. In (Diamond and Leeman 1995) pore sizes down to $8{\times}10^{-7}$m are reported. Additionally, a comparison of pore-size distributions obtained from SEM micrographs and the respective distributions from MIP measurements is given in (Diamond and Leeman 1995). The comparison clearly shows the aforementioned underestimation of the portion of larger pore sizes when employing MIP [see Figure 7(b)].

Figure 7(a) shows typical data obtained from MIP and image analysis of vacuum mixed cement pastes, characterized by no initial porosity, i.e., $f_g(\xi = 0) = 0$. Taking into account that MIP measurements provide reliable results for small pore sizes and image analysis is limited to greater pore-size ranges, a line approximating the respective ranges of the pore size is introduced [see Figure 7(b)]. Based on experimental data of cement pastes characterized by various values of the w/c-ratio and ξ (Cook and Hover 1999; Diamond and Leeman 1995), the slope of the line was identified as $k = 0.2/\log_{10}(3 \times 10^{-7}/1 \times 10^{-8}) = 0.135$, starting from a pore diameter of $2.5{\times}10^{-9}$m. According to (Bye 1999), the latter corresponds to the smallest pore size, at which menisci can form. The linear approximation of the cumulative pore-size distribution allows to determine the pore radius at the liquid-gas interface for a given volume fraction of the gaseous phase $f_g(\xi, w/c)$ [see Figure 7(b)]. For the so-obtained value of $2R_w(f_g)$, the capillary depression of the pore liquid can be computed from Equation (7).

This approach was assessed by four different data sets reported in the open literature (Acker 2001; Hua et al. 1995; Cook and Hover 1999; Jehng et al. 1996). Figure 8 shows the comparison of these test data and the model prediction based on $k = 0.135$. The model result for Δp_l as a function of the w/c-ratio and ξ were obtained from the calculation scheme outlined in Table 1.

3 CONTINUUM MICROMECHANICAL MODEL

The framework of continuum micromechanics is proposed to predict autogenous-shrinkage strains at the macroscale. After identification of the material
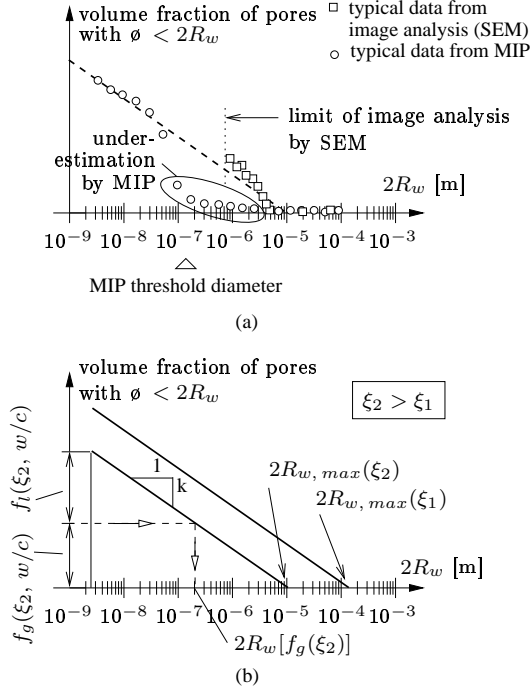
(a)

(b)

Figure 7: Cumulative pore-size distributions: (a) typical experimental data, (b) line, fitting experimental data [see also (Koenders and van Breugel 1998)]

□ MIP data by Acker (2001)
△ MIP data by Hua et al. (1995), w/c=0.42
○ MIP data by Cook and Hover (1999)
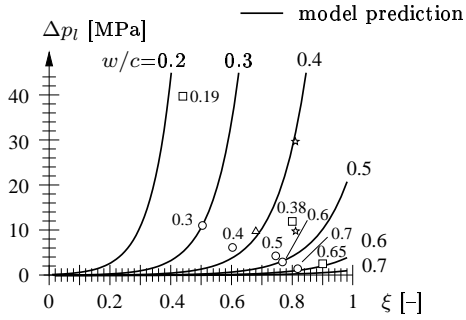⋆ NMR data by Jehng et al. (1996), w/c=0.43

Figure 8: Capillary depression of the pore liquid as a function of the w/c-ratio and ξ

phases at the different scales of observation, the elastic properties and, finally, the autogenous-shrinkage deformations will be upscaled.

3.1 Representation

First, the different phases in a representative volume element (RVE) need to be identified. A phase

in terms of continuum micromechanics constitutes a material domain with constant material properties at a given length scale. In this work, three length scales are considered. The phases at the different length scales are identified as follows:

- At the cement-paste scale, water, yet unhydrated (anhydrous) cement, reaction products, and capillary pores, either filled with liquid or gas, are forming a polycrystal.

- At the aggregate scale, aggregates are represented as spherical inclusions in the cement paste.

- Finally, at the macroscale, concrete is treated as a continuum.

The three length scales obey the separability of scale condition, i.e., they are separated one from another by at least one order of magnitude.

3.1.1 The cement-paste scale

The volume fractions f_r at the cement-paste scale are defined as functions of the w/c-ratio and the degree of hydration ξ (Acker 2001) (see Figure 1):

$$
\begin{aligned}
f_c(\xi) &= (1-\xi) \times f_c(\xi=0) , \\
f_h(\xi) &= 2.16 \times [f_c(\xi=0) - f_c(\xi)] , \\
f_g(\xi) &= 0.18 \times [f_c(\xi=0) - f_c(\xi)] + f_{g0} , \\
f_l(\xi) &= f_c(\xi=0) \times w/c \times \rho_c/\rho_l \\
&\quad -1.34 \times [f_c(\xi=0) - f_c(\xi)] \geq 0 ,
\end{aligned}
\tag{8}
$$

with $f_c(\xi) + f_h(\xi) + f_g(\xi) + f_l(\xi) = 1$. f_c, f_h, f_g and f_l denote the volume fractions of cement, hydrates, the gaseous phase, and the liquid phase, re-

Table 1: Determination of Δp_l for specific values of the w/c-ratio and ξ

1. Determination of f_l and f_g on the basis of the linear relations given in Figure 1 (see also Subsection 3.1).

2. Use of linear relationship in Figure 7(b), defined by the computed values for $f_g + f_l$ at $2R_w = 2.5 \times 10^{-9}$ m and the slope $k = 0.135 = $ const., for determination of $2R_{w,max}$ and $2R_w(f_g)$ from

$$
k = \frac{f_g + f_l}{\log_{10}(2R_{w,max}) - \log_{10}(2.5 \times 10^{-9})}
$$

$$
k = \frac{f_g}{\log_{10}(2R_{w,max}) - \log_{10}(2R_w(f_g))}
$$

3. Determination of Δp_l from $2R_w(f_g)$ using Equation (7)

spectively. In Equation (8), ρ_c/ρ_l is the ratio of cement to liquid density, with $\rho_c/\rho_l = 3.15$ (Acker 2001), the numbers 2.16, 0.18, and 1.34 were computed from $(1 + \overline{w/c} \times \rho_c/\rho_l) \times (100\% - 7.7\%)$, $(1 + \overline{w/c} \times \rho_c/\rho_l) \times 7.7\%$, and $\overline{w/c} \times \rho_c/\rho_l$, where 7.7% represents the volumetric imbalance in the course of hydration (*Le Chatelier* contraction) and $\overline{w/c} = 0.425$ (Acker 2001). f_{g0} denotes the volume fraction of the gaseous phase introduced during the mixing process (entrained air). Figure 1 shows the evolution of the volume fractions given in Equations (8) as a function of ξ. Depending on the w/c-ratio, three cases are distinguished:

- Cement pastes characterized by $w/c = \overline{w/c} = 0.425$ hydrate completely, i.e., all cement clinker is consumed. No water is present at $\xi = 1$ (see Figure 1).

- Pastes with $w/c < \overline{w/c}$ cannot hydrate completely. The chemical reaction stops by the time all liquid has been consumed. Accordingly, ξ remains smaller than one.

- Pastes characterized by $w/c > \overline{w/c}$ hydrate completely. The larger the w/c-ratio, the more liquid is present at $\xi = 1$.

3.1.2 *The aggregate scale*

The volume fractions f_r at the aggregate scale are defined as follows:

- f_p denotes the volume fraction of the cement paste.

- f_a is the volume fraction of aggregates.

The sum of f_p and f_a must be equal to 1.

3.2 *Localization & homogenization of elastic properties*

For determination of macroscopic elastic properties of early-age concrete, a recently published homogenization scheme by (Bernard et al. 2003) is employed. Whereas four scales of observation below the macroscale were introduced in (Bernard et al. 2003), requiring four homogenization steps for the upscale of elastic properties, only two homogenization steps are required when using the material representation introduced in Subsection 3.1. Similar to (Bernard et al. 2003), homogenization at the cement-paste scale is performed using the generalized self consistent scheme (Hershey 1954; Kröner 1958), whereas the Mori-Tanaka scheme is used for homogenization of the cement paste / aggregate compound, finally providing the macroscopic elastic properties. The intrinsic properties of the different material phases employed in this paper are listed in Table 2.

Table 2: Bulk modulus k and shear modulus μ for the single phases [average values taken from (Acker 2001)]

cement paste scale		
phase	k [GPa]	μ [GPa]
anhydrous cement	117	54
liquid phase	2.3	0
gaseous phase	0	0
hydrates	14	9

3.3 *Homogenization of autogenous-shrinkage deformation*

Homogenization of elastic properties (Subsection 3.2) is characterized by the assumption that each hydrate formed in the course of the hydration process contributes equally to the macroscopic elasticity tensor $\mathbf{C}(\xi)$ by its intrinsic stiffness properties (see Table 2). At the macroscopic scale, the stress-free formation of hydrates [the hydrates are not loaded when they are formed (Bažant 1979)] is standardly considered by an infinitesimal stress-strain law [see, e.g., (Sercombe et al. 2000; Lackner et al. 2002)], reading

$$d\boldsymbol{\sigma} = \mathbf{C}(\xi) : d\boldsymbol{\varepsilon} \,, \qquad (9)$$

where $\mathbf{C}(\xi) = \mathbf{C}_{hom}^{II}(\xi)$ is the elasticity tensor of the material at the macroscopic scale of observation. At this scale, autogenous shrinkage is considered by extending Equation (9) to

$$d\boldsymbol{\sigma} = \mathbf{C}(\xi) : [d\boldsymbol{\varepsilon} - d\boldsymbol{\varepsilon}^s(\xi)] \,, \qquad (10)$$

where $\boldsymbol{\varepsilon}^s(\xi)$ represents the yet unknown macroscopic autogenous-shrinkage strain tensor corresponding to a situation free of macrostress. Accordingly, no macrostress is applied in the subsequent determination of $\boldsymbol{\varepsilon}^s(\xi)$ by means of homogenization. However, the hydrating cement at finer scales of observation becomes loaded, resulting from the capillary depression of the liquid phase. Similar to the infinitesimal approach at the macroscopic scale of observation [see Equations (9) and (10)], newly-formed hydrates do not affect the autogenous-shrinkage strains developed so far at finer scales of observation. Within the framework of continuum micromechanics, this situation is accounted for by an infinitesimal approach, continuously introducing additional hydrate phases, df_h (see Figure 9). Each hydrate phase is loaded exclusively by changes in the capillary depression, $d(\Delta p_l)$, occurring *after* formation of the respective phase. In the context of this infinitesimal approach, the stress-strain law in the liquid phase V_l at the cement-paste scale takes the form

$$V_l \,:\, d\boldsymbol{\sigma} \;=\; \mathbf{C}_l : (d\boldsymbol{\varepsilon}^0 + d\boldsymbol{\varepsilon}_l - d\bar{\boldsymbol{\varepsilon}}_l) \,, \quad (11)$$
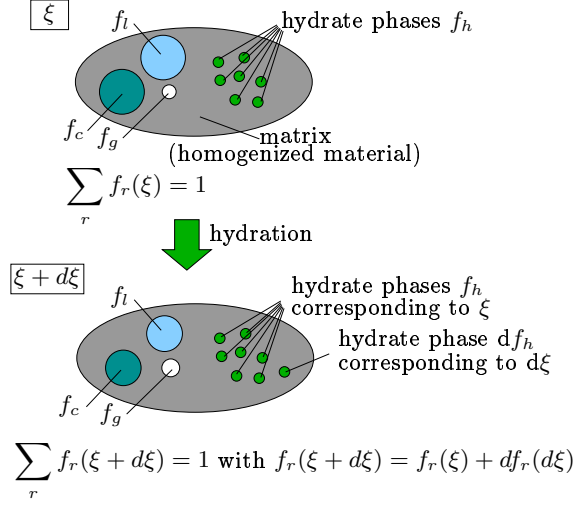
Figure 9: Change of phase composition resulting from infinitesimal change of hydration products, df_h, allowing to account for stress-free formation of hydrates at the cement-paste scale
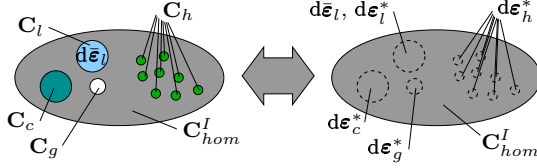

Figure 10: Equivalent inclusion: material tensors $\mathbf{C}_r$ are replaced by $\mathbf{C}_{hom}^I$, constant eigenstrains $d\boldsymbol{\varepsilon}_r^*$ are introduced in the inclusions

where the strain tensor is composed of a constant part $d\boldsymbol{\varepsilon}^0$ and a variable part $d\boldsymbol{\varepsilon}_l$. In Equation (11), the strain tensor $d\bar{\boldsymbol{\varepsilon}}_l$ is introduced in order to account for the applied load in consequence of capillary depression, with $d\bar{\boldsymbol{\varepsilon}}_l = -\mathbf{1}d(\Delta p_l)/(3k_l)$, where Δp_l is obtained from the degree of hydration as outlined in Table 1. Within the self-consistent scheme, the material tensor $\mathbf{C}_l$ for the liquid phase in Equation (11) is replaced by the homogenized material tensor $\mathbf{C}_{hom}^I$, reading

$$d\boldsymbol{\sigma} \;=\; \mathbf{C}_{hom}^I : (d\boldsymbol{\varepsilon}^0 + d\boldsymbol{\varepsilon}_l - d\boldsymbol{\varepsilon}_l^* - d\bar{\boldsymbol{\varepsilon}}_l), \quad (12)$$

where the introduction of the constant tensor of eigenstrains $d\boldsymbol{\varepsilon}_l^*$ (constant in V_l) compensates the change of material properties (see Figure 10). The variable part of the strain tensor $d\boldsymbol{\varepsilon}_l$ in Equation (12) is a function of $d\boldsymbol{\varepsilon}_l^{**}$, with $d\boldsymbol{\varepsilon}_l^{**} = d\boldsymbol{\varepsilon}_l^* + d\bar{\boldsymbol{\varepsilon}}_l$. According to (Eshelby 1957), it is obtained as

$$d\boldsymbol{\varepsilon}_l = \mathbf{S}_l : d\boldsymbol{\varepsilon}_l^{**} , \quad (13)$$

where $\mathbf{S}_l$ denotes the fourth-order Eshelby tensor. (Eshelby 1957) showed that in case of an ellipsoidal

inclusion V_l, $\mathbf{S}_l$ and, hence, $d\boldsymbol{\varepsilon}_l$ is constant in V_l. Consideration of Equation (13) in the stress-strain laws (11) and (12),

$$\begin{aligned} V_l : \quad & \mathbf{C}_l : [d\boldsymbol{\varepsilon}^0 + \mathbf{S}_l : d\boldsymbol{\varepsilon}_l^{**} - d\bar{\boldsymbol{\varepsilon}}_l] \\ = \; & \mathbf{C}_{hom}^I : [d\boldsymbol{\varepsilon}^0 + (\mathbf{S}_l - \mathbf{I}) : d\boldsymbol{\varepsilon}_l^{**}] , \end{aligned}$$
$$(14)$$

yields an expression for $d\boldsymbol{\varepsilon}_l^{**}$ in the form:

$$\begin{aligned} d\boldsymbol{\varepsilon}_l^{**} \;=\; & [(\mathbf{C}_l - \mathbf{C}_{hom}^I) : \mathbf{S}_l + \mathbf{C}_{hom}^I]^{-1} : \\ & [(\mathbf{C}_{hom}^I - \mathbf{C}_l) : d\boldsymbol{\varepsilon}^0 + \mathbf{C}_l d\bar{\boldsymbol{\varepsilon}}_l] . \end{aligned}$$
$$(15)$$

The infinitesimal stress-strain law in the remaining phases r, with $r \in \{c, g, h\}$, is given as

$$\begin{aligned} V_r : \quad d\boldsymbol{\sigma} \;=\; & \mathbf{C}_r : (d\boldsymbol{\varepsilon}^0 + d\boldsymbol{\varepsilon}_r) \\ =\; & \mathbf{C}_{hom}^I : (d\boldsymbol{\varepsilon}^0 + d\boldsymbol{\varepsilon}_r - d\boldsymbol{\varepsilon}_r^*) . \end{aligned}$$
$$(16)$$

Consideration of $d\boldsymbol{\varepsilon}_r = \mathbf{S}_r : d\boldsymbol{\varepsilon}_r^*$ in Equation (16) yields

$$\begin{aligned} d\boldsymbol{\varepsilon}_r^* \;=\; & [(\mathbf{C}_r - \mathbf{C}_{hom}^I) : \mathbf{S}_r + \mathbf{C}_{hom}^I]^{-1} : \\ & [(\mathbf{C}_{hom}^I - \mathbf{C}_r) : d\boldsymbol{\varepsilon}^0] . \end{aligned}$$
$$(17)$$

Based on $\langle d\boldsymbol{\sigma} \rangle_V = \mathbf{0}$, which follows from $\langle \boldsymbol{\sigma} \rangle_V = \mathbf{0}$ in the situation free of macrostress, one gets

$$\begin{aligned} V : \quad \mathbf{0} \;=\; & f_l \mathbf{C}_{hom}^I : [d\boldsymbol{\varepsilon}^0 + (\mathbf{S}_l - \mathbf{I}) : d\boldsymbol{\varepsilon}_l^{**}] \\ + \; & f_c \mathbf{C}_{hom}^I : [d\boldsymbol{\varepsilon}^0 + (\mathbf{S}_c - \mathbf{I}) : d\boldsymbol{\varepsilon}_c^*] \\ + \; & f_g \mathbf{C}_{hom}^I : [d\boldsymbol{\varepsilon}^0 + (\mathbf{S}_g - \mathbf{I}) : d\boldsymbol{\varepsilon}_g^*] \\ + \; & \int_0^{f_h} \mathbf{C}_{hom}^I : [d\boldsymbol{\varepsilon}^0 + (\mathbf{S}_h - \mathbf{I}) : d\boldsymbol{\varepsilon}_h^*] df_h . \end{aligned}$$
$$(18)$$

Considering Equations (15) and (17) in Equation (18), the constant part of the strain tensor $d\boldsymbol{\varepsilon}^0$ is obtained as a function of $d\bar{\boldsymbol{\varepsilon}}_l$ in the form

$$d\boldsymbol{\varepsilon}^0 = -\boldsymbol{\Lambda}^{-1} : \boldsymbol{\Gamma}_l : d\bar{\boldsymbol{\varepsilon}}_l , \quad (19)$$

where the fourth-order tensors $\boldsymbol{\Lambda}$ and $\boldsymbol{\Gamma}_l$ contain the volume fractions f_r, the Eshelby tensors $\mathbf{S}_r$, and the elasticity tensors of the different phases as well as the homogenized material tensor (see Appendix). The infinitesimal macroscopic total strain tensor $d\bar{\boldsymbol{\varepsilon}}_{hom}^I$ for an infinitesimal increase of the hydrate phase, df_h, is obtained from the volume average of the strain field $d\boldsymbol{\varepsilon}^0 + d\boldsymbol{\varepsilon}$, reading

$$\begin{aligned} d\bar{\boldsymbol{\varepsilon}}_{hom}^I \;=\; & \int_V (d\boldsymbol{\varepsilon}^0 + d\boldsymbol{\varepsilon}) dV = \\ =\; & d\boldsymbol{\varepsilon}^0 + f_l \langle d\boldsymbol{\varepsilon}_l \rangle_{V_l} + f_c \langle d\boldsymbol{\varepsilon}_c \rangle_{V_c} \\ & + f_g \langle d\boldsymbol{\varepsilon}_g \rangle_{V_g} + \int_0^{f_h} \langle d\boldsymbol{\varepsilon}_h \rangle_{V_h} df_h \\ =\; & d\boldsymbol{\varepsilon}^0 + f_l \mathbf{S}_l : d\boldsymbol{\varepsilon}_l^{**} + f_c \mathbf{S}_c : d\boldsymbol{\varepsilon}_c^* \\ & + f_g \mathbf{S}_g : d\boldsymbol{\varepsilon}_g^* + \int_0^{f_h} \mathbf{S}_h : d\boldsymbol{\varepsilon}_h^* df_h \\ =\; & (\mathbf{I} + \boldsymbol{\Xi}) : d\boldsymbol{\varepsilon}^0 + \boldsymbol{\Theta}_l : d\bar{\boldsymbol{\varepsilon}}_l , \end{aligned}$$
$$(20)$$

where the expressions for $\mathbf{\Xi}$ and $\mathbf{\Theta}_l$ are given in the Appendix. Considering Equation (19) and $d\bar{\varepsilon}_l = -\mathbf{1}d(\Delta p_l)/(3k_l)$ in Equation (20), one gets

$$d\bar{\varepsilon}^I_{hom} = [(\mathbf{I}+\mathbf{\Xi}):\mathbf{\Lambda}^{-1}:\mathbf{\Gamma}_l - \mathbf{\Theta}_l]:\mathbf{1}d(\Delta p_l)/(3k_l) .\tag{21}$$
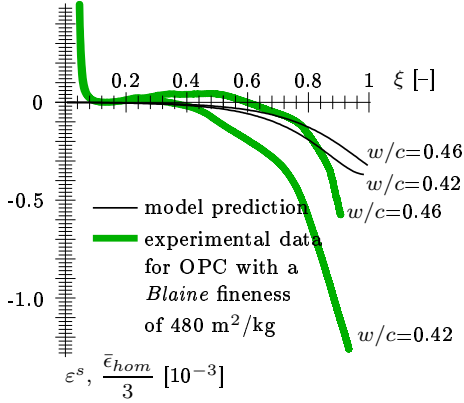

Figure 11: Comparison of results obtained from continuum-micromechanical model with experimental data

Accounting for the isotropic character of the capillary depression in the liquid phase and, hence, of the prescribed strain $d\bar{\varepsilon}^I_{hom}$, Equation (21) can be written in volumetric form as

$$d\bar{\epsilon}^I_{hom} = [(1 + \Xi)\Lambda^{-1}\Gamma_l - \Theta_l]d(\Delta p_l)/k_l .\tag{22}$$

Ξ, Λ, Γ_l, and Θ_l are given in the Appendix and $S = 1/3(1 + \nu^I_{hom})/(1 - \nu^I_{hom})$ (see Appendix). Homogenization of autogenous shrinkage strains at the aggregate scale is performed by prescribing shrinkage strains $d\bar{\varepsilon}^I_{hom}$ in the cement-paste phase following the procedure outlined in (Pichler et al. 2003).

4 COMPARISON WITH EXPERIMENTAL RESULTS

The multi-scale model presented in the previous section was employed for re-analysis of one-dimensional autogenous-shrinkage experiments conducted at Vienna University of Technology. In the respective testing program, three types of cement characterized by various *Blaine* fineness with varying w/c-ratios were considered. Figure 3 shows the obtained histories for the uniaxial strain. Combination of these data with the chemical affinity $\tilde{A}(\xi)$ computed in Subsection 2.1 gives access to the autogenous-shrinkage strain as a function of ξ. From comparison of the so-obtained material function $\varepsilon^s(\xi)$ with the prediction of the multi-scale model $\bar{\epsilon}^I_{hom}(\xi)/3$, the following conclusions can be drawn: Whereas the described homogenization approach is capable to qualitatively describe autogenous shrinkage of cement-based materials, the magnitude of autogenous-shrinkage strains is underestimated. This may be explained by the underlying elastic behavior of the single constituents assumed in the employed homogenization approach. Experimental results [see, e.g., (Acker 2001)], as well as theoretical considerations [see, e.g., (Bažant et al. 1997)] suggest to extend the proposed homogenization approach to creep. Future work will include the identification of the governing creep process in the hydrate phase. The proposed infinitesimal homogenization scheme will allow to incorporate these results, accounting for the different load histories of hydrate phases formed at different instants of time.

5 CONCLUDING REMARKS AND OUTLOOK

Starting with the identification of the pore structure, a linear relationship between the accumulative pore space and the pore diameter in logarithmic scale was introduced [similar to (Koenders and van Breugel 1998)]. Surprisingly, this rather simple approximation defining the pore size distribution and, hence, the capillary depression at various extents of the hydration process showed good agreement with experimental data, accounting for the large scatter present in such experiments. Even though an infinitesimal homogenization approach was chosen for upscaling autogenous-shrinkage deformations, accounting for the stress-free formation of new hydrates at finer scales of observation, the experimental results obtained from uniaxial shrinkage tests were still underestimated. This was explained by the underlying assumption of linear elastic material behavior of the different material phases. Future work will be devoted to the extension of the proposed homogenization scheme to finer-scale creep of hydrates; respective experiments are in progress.

Before the obtained material function for autogenous shrinkage may be used in the context of macroscopic analyses accounting for chemomechanical couplings (Ulm and Coussy 1996; Hellmich et al. 1999; Lackner et al. 2002; Pichler et al. 2003), verification of the second homogenization step from the aggregate scale to the macroscale is required. For this purpose, the uniaxial autogenous-shrinkage experiments conducted with cement pastes will be extended to mortar.

Hence, finally the prediction of the influence of autogenous shrinkage on the response of real-life structures will become possible. The optimization of concrete mixtures for specific applications, aiming at a reduction of the deformations caused by autogenous-shrinkage represents the far-goal of this research.

APPENDIX

For the sake of clarity of the description of the micromechanical model, the following symbols were introduced:

$$\begin{aligned}
\mathbf{\Lambda} = \mathbf{I} \; + \; & f_l(\mathbf{S}_l - \mathbf{I}) : [(\mathbf{C}_l - \mathbf{C}_{hom}^I) : \mathbf{S}_l \\
& + \mathbf{C}_{hom}^I]^{-1} : (\mathbf{C}_{hom}^I - \mathbf{C}_l) \\
+ \; & f_c(\mathbf{S}_c - \mathbf{I}) : [(\mathbf{C}_c - \mathbf{C}_{hom}^I) : \mathbf{S}_c \\
& + \mathbf{C}_{hom}^I]^{-1} : (\mathbf{C}_{hom}^I - \mathbf{C}_c) \\
+ \; & f_g(\mathbf{S}_g - \mathbf{I}) : [(\mathbf{C}_g - \mathbf{C}_{hom}^I) : \mathbf{S}_g \\
& + \mathbf{C}_{hom}^I]^{-1} : (\mathbf{C}_{hom}^I - \mathbf{C}_g) \\
+ \; & \int_0^{f_h} (\mathbf{S}_h - \mathbf{I}) : [(\mathbf{C}_h - \mathbf{C}_{hom}^I) : \mathbf{S}_h \\
& + \mathbf{C}_{hom}^I]^{-1} : (\mathbf{C}_{hom}^I - \mathbf{C}_h)df_h
\end{aligned} \tag{23}$$

$$\mathbf{\Gamma}_l = f_l(\mathbf{S}_l - \mathbf{I}) : [(\mathbf{C}_l - \mathbf{C}_{hom}) : \mathbf{S}_l \\ + \mathbf{C}_{hom}^I]^{-1} : \mathbf{C}_l \tag{24}$$

$$\begin{aligned}
\mathbf{\Xi} = \; & f_l\mathbf{S}_l : [(\mathbf{C}_l - \mathbf{C}_{hom}^I) : \mathbf{S}_l \\
& + \mathbf{C}_{hom}^I]^{-1} : [(\mathbf{C}_{hom}^I - \mathbf{C}_l)] \\
+ \; & f_c\mathbf{S}_c : [(\mathbf{C}_c - \mathbf{C}_{hom}^I) : \mathbf{S}_c \\
& + \mathbf{C}_{hom}^I]^{-1} : [(\mathbf{C}_{hom}^I - \mathbf{C}_c)] \\
+ \; & f_g\mathbf{S}_g : [(\mathbf{C}_g - \mathbf{C}_{hom}^I) : \mathbf{S}_g \\
& + \mathbf{C}_{hom}^I]^{-1} : [(\mathbf{C}_{hom}^I - \mathbf{C}_g)] \\
+ \; & \int_0^{f_h} \mathbf{S}_h : [(\mathbf{C}_h - \mathbf{C}_{hom}^I) : \mathbf{S}_h \\
& + \mathbf{C}_{hom}^I]^{-1} : [(\mathbf{C}_{hom}^I - \mathbf{C}_h)]df_h
\end{aligned} \tag{25}$$

$$\mathbf{\Theta}_l = f_l\mathbf{S}_l : [(\mathbf{C}_l - \mathbf{C}_{hom}^I) : \mathbf{S}_l \\ + \mathbf{C}_{hom}^I]^{-1} : \mathbf{C}_l \tag{26}$$

$$\begin{aligned}
\Lambda = 1 \; + \; & f_l(S - 1)[(k_l - k_{hom}^I)S \\
& + k_{hom}^I]^{-1}(k_{hom}^I - k_l) + \\
+ \; & f_c(S - 1)[(k_c - k_{hom}^I)S \\
& + k_{hom}^I]^{-1}(k_{hom}^I - k_c) + \\
+ \; & f_g(S - 1)[(k_g - k_{hom}^I)S \\
& + k_{hom}^I]^{-1}(k_{hom}^I - k_g) + \\
+ \; & \int_0^{f_h} (S - 1)[(k_h - k_{hom}^I)S \\
& + k_{hom}^I]^{-1}(k_{hom}^I - k_h)df_h
\end{aligned} \tag{27}$$

$$\Gamma_l = f_l(S - 1)[(k_l - k_{hom})S \\ + k_{hom}^I]^{-1}k_l \tag{28}$$

$$\begin{aligned}
\Xi = \; & f_lS[(k_l - k_{hom}^I)S + k_{hom}^I]^{-1} \\
& [(k_{hom}^I - k_l)] \\
+ \; & f_cS[(k_c - k_{hom}^I)S + k_{hom}^I]^{-1} \\
& [(k_{hom}^I - k_c)] \\
+ \; & f_gS[(k_g - k_{hom}^I)S + k_{hom}^I]^{-1} \\
& [(k_{hom}^I - k_g)] \\
+ \; & \int_0^{f_h} S[(k_h - k_{hom}^I)S + k_{hom}^I]^{-1} \\
& [(k_{hom}^I - k_h)]df_h
\end{aligned} \tag{29}$$

$$\Theta_l = f_lS[(k_l - k_{hom}^I)S + k_{hom}^I]^{-1}k_l \tag{30}$$

In Equations (27) to (30), S denotes the remaining part of the Eshelby tensor $\mathbf{S}$, specialized for spherical inclusions (see, e.g., (Nemat-Nasser and Hori 1993))

$$\begin{aligned}
S_{ijkl} = \; & \frac{5\nu_{hom}^I - 1}{15(1 - \nu_{hom}^I)}\delta_{ij}\delta_{kl} \\
& + \frac{4 - 5\nu_{hom}^I}{15(1 - \nu_{hom}^I)}(\delta_{ik}\delta_{jl} + \delta_{il}\delta_{jk}) \,,
\end{aligned} \tag{31}$$

giving $S = S_{iiii} + 2\,S_{iijj} = 1/3\,(1 + \nu_{hom}^I)/(1 - \nu_{hom}^I)$, where ν_{hom}^I denotes Poisson's ratio of the homogenized material.

REFERENCES

Acker, P. (2001). Micromechanical analysis of creep and shrinkage mechanisms. In F.-J. Ulm, Z. Bažant, and F. Wittmann (Eds.), *Proceedings of the 6th International Conference on Creep, Shrinkage & Durability Mechanics of Concrete and other Quasi-Brittle Materials*, Cambridge, USA, pp. 15–25. Elsevier Science Ltd., Amsterdam.

Acker, P. and F.-J. Ulm (2001). Creep and shrinkage of concrete: physical origins and practical measurements. *Nuclear Engineering and Design 203*, 148 – 158.

Ballim, Y. and P. Graham (2003). Early-age heat evolution of clinker cements in relation to microstructure and composition: implications for temperature development in large concrete elements. *Cement & Concrete Composites*. In press.

Bažant, Z. (1979). Thermodynamics of solidifying or melting viscoelastic material. *Journal of the Engineering Mechanics Division, ASCE 105*(6), 933–952.

Bažant, Z., A. Hauggard, S. Baweja, and F.-J. Ulm (1997). Microprestress solidification theory for concrete creep, part I: Aging and drying effects. *Journal of Engineering Mechanics, ASCE 123*(11), 1188–1194.

Bernard, O., F.-J. Ulm, and E. Lemarchand (2003). A multiscale micromechanics-hydration model for the early-age elastic properties of cement-based materials. *Cement and Concrete Research 33*, 1293–1309.

Bye, G. (1999). *Portland Cement* (2 ed.). London, England: Thomas Telford Publishing.

Cook, R. and K. Hover (1999). Mercury porosimetry of hardened cement paste. *Cement and Concrete Research 29*, 993–943.

Diamond, S. (2000). Review mercury porosimetry: An inappropriate method for the measurement of pore size distributions in cement-based materials. *Cement and Concrete Research 30*, 1517–1525.

Diamond, S. and M. Leeman (1995). Pore size distribution in hardened cement paste by SEM image analysis. In S. Diamond, S. Mindess, F. Glasser, L. Roberts, J. Skalny, and L. Wakely (Eds.), *Microstructure of Cement-based systems / Bonding and Interfaces in Cementitious Materials*, Volume 370, pp. 217 – 226. Materials Research Society, Pittsburgh.

Eshelby, J. (1957). The determination of the elastic field of an ellipsoidal inclusion, and related problems. *Proceedings of the Royal Society of London A 241*, 376–396.

Freiesleben Hansen, P. and E. Pedersen (1977). Måleinstrument til kontrol af betons hardening [Measurement device for controlling hardening of concrete]. *Nordisk Betong 1*, 21–25.

Gaydos, J., L. Boruvka, Y. Rotenberg, P. Chen, and A. Neumann (1996). *Applied Surface Thermodynamics*. Dekker, New York.

Hellmich, C., F.-J. Ulm, and H. A. Mang (1999). Multisurface chemoplasticity I: Material model for shotcrete. *Journal of Engineering Mechanics (ASCE) 125*(6), 692–701.

Hershey, A. (1954). The elasticity of an isotropic aggregate of anisotropic cubic crystals. *Journal of Applied Mechanics (ASME) 21*, 236–240.

Hornak, J. (2003). The basics of NMR, online manual of the Magnetic Resonance Laboratory, Rochester Institute of Technology, http://www.cis.rit.edu/htbooks/nmr.

Hua, C., P. Acker, and A. Ehrlacher (1995). Analyses and models of the autogenous shrinkage of hardening cement paste I. Modelling at macroscopic scale. *Cement and Concrete Research 25*, 1457–1468.

Jehng, J.-Y., D. Sprague, and W. Halperin (1996). Pore structure of hydrating cement paste by magnetic resonance relaxation analysis and freezing. *Magnetic Resonance Imaging 14*, 785 – 791.

Jensen, O. and P. Freiesleben Hansen (1995). A dilatometer for measuring autogenous deformation in hardening Portland cement paste. *Materials and Structures 28*(181), 69–76.

Jensen, O. and P. Freiesleben Hansen (2001). Autogenous deformation and RH-change in perspective. *Cement and Concrete Research 31*, 1859–1865.

Koenders, E. and K. van Breugel (1998). Numerical modelling of self-desiccation of hardening cement paste. *HERON 43*(2), 99 – 118.

Kröner, E. (1958). Berechnung der elastischen Konstanten des Vielkristalls aus den Konstanten des Einkristalls [Computation of the elastic constants of a polycrystal based on the constants of the single crystal]. *Zeitschrift für Physik 151*, 504–518. In German.

Lackner, R., C. Hellmich, and H. Mang (2002). Constitutive modeling of cementitious materials in the framework of chemoplasticity. *International Journal for Numerical Methods in Engineering 53*(10), 2357–2388.

Milia, F., M. Fardis, G. Papavassiliou, and A. Leventis (1998). NMR in porous materials. *Magnetic Resonance Imaging 16*, 677 – 678.

Nemat-Nasser, S. and M. Hori (1993). *Micromechanics: overall properties of heterogeneous materials*, Volume 37. North-Holland, Amsterdam.

Pichler, C., R. Lackner, and H. Mang (2003). Continuum-micromechanics approach for determination of frost heave in artificial ground freezing. In K. Bathe (Ed.), *Proceedings of the 2nd MIT Conference on Computational Fluid and Solid Mechanics*, pp. 578–581. Elsevier Science Ltd., Oxford.

Pichler, C., R. Lackner, Y. Spira, and H. Mang (2003). Thermochemomechanical assessment of ground improvement by jet grouting in tunneling. *Journal of Engineering Mechanics (ASCE) 129*(8), 951–962.

Sercombe, J., C. Hellmich, F.-J. Ulm, and H. A. Mang (2000). Modeling of early-age creep of shotcrete. I: model and model parameters. *Journal of Engineering Mechanics (ASCE) 126*(3), 284–291.

Ulm, F.-J. and O. Coussy (1995). Modeling of thermochemomechanical couplings of concrete at early ages. *Journal of Engineering Mechanics (ASCE) 121*(7), 785–794.

Ulm, F.-J. and O. Coussy (1996). Strength growth as chemo-plastic hardening in early age concrete. *Journal of Engineering Mechanics (ASCE) 122*(12), 1123–1132.